AD-A047 632 GENERAL ELECTRIC CO SYRACUSE N Y HEAVY MILITARY EQUI--ETC F/G 20/5
A PRELIMINARY ANALYSIS OF THE PERFORMANCE OF THE UNIVERSITY OF --ETC(U)
OCT 77 G T BURNHAM

UNCLASSIFIED R77EMH12 NL

| OF |
AD
A047632

END
DATE
FILMED
1 -78
DDC

GENERAL ELECTRIC

HEAVY MILITARY EQUIPMENT DEPARTMENT

TECHNICAL INFORMATION SERIES

Author	Subject Category	No.
G. T. Burnham	Neodymium Glass Fusion Laser Systems	R77EMH12
		Date Oct 1977

Title

A PRELIMINARY ANALYSIS OF THE PERFORMANCE OF THE UNIVERSITY OF ROCHESTER'S GLASS DEVELOPMENT LASER.

Copies Available at	GE Class	No. of Pages
HMED TIS Distribution Center Box 4840 (CSP 4-18) Syracuse, New York 13221	1	28
	Govt Class: Unclassified	

Summary

The results of a three-dimensional computer code analysis of the University of Rochester's Glass Development Laser through the 90-mm diameter rod amplifier stage is presented. Through the use of re-imaging optics (via vacuum spatial filtering) system outputs as well as performance prediction capabilities are considerably improved.

408 969

Send to _____

GENERAL ELECTRIC COMPANY TECHNICAL INFORMATION

Within the limitations imposed by Government data export regulations and security classifications, the availability of General Electric Company technical information is regulated by the following classifications in order to safeguard proprietary information:

CLASS 1: GENERAL INFORMATION

Available to anyone on request.
Patent, legal and commercial review required before issue.

CLASS 2: GENERAL COMPANY INFORMATION

Available to any General Electric Company employee on request.
Available to any General Electric Subsidiary or Licensee subject to existing agreements.
Disclosure outside General Electric Company requires approval of originating component.

CLASS 3: LIMITED AVAILABILITY INFORMATION

Original Distribution to those individuals with specific need for information.
Subsequent Company availability requires originating component approval.
Disclosure outside General Electric Company requires approval of originating component.

CLASS 4: HIGHLY RESTRICTED DISTRIBUTION

Original distribution to those individuals personally responsible for the Company's interests in the subject.
Copies serially numbered, assigned and recorded by name.
Material content, and knowledge of existence, restricted to copy holder.

GOVERNMENT SECURITY CLASSIFICATIONS, when required, take precedence in the handling of the material. Wherever not specifically disallowed, the General Electric classifications should also be included in order to obtain proper handling routines.

HMED 4023B (5-65)

GENERAL ELECTRIC COMPANY
HEAVY MILITARY EQUIPMENT DEPARTMENT
TECHNICAL INFORMATION SERIES

SECTION Advanced Development Engineering

UNIT Advanced Electro Optics

HMED ACCOUNTING REFERENCE 575

COLLABORATORS

APPROVED D. M. Gall TITLE Mgr., Adv Electro Optics LOCATION CSP 4-49

R77EMH12

MINIMUM DISTRIBUTION - Government Unclassified Material (and Title Pages) in G.E. Classes 1, 2, or 3 will be the following.

Copies	Title Page Only	To
0	1	Legal Section, HMED (Syracuse)
0	1	Manager, Technological Planning, HMED (Syracuse)
5	6	G-E Technical Data Center (Schenectady)

MINIMUM DISTRIBUTION - Government Classified Material, Secret or Confidential in G.E. Classes 1, 2, or 3 will be the following.

1	1	Classified Section, Electronics Park Library
1	0	Manager, Technological Planning, HMED (Syracuse)

ADDITIONAL DISTRIBUTION (Keep at minimum within intent of assigned G.E. Class.)

COPIES	NAME	LOCATION
5 (CLASS 1 ONLY)	DEFENSE DOCUMENTATION CENTER	CAMERON STATION, ALEXANDRIA, VA. 22314
1	L. I. Chasen	P.O. Box 8555 Philadelphia, Pa., 19101
1	Balian, E.S.	CSP 3-12
1	Bakeman, O.R.	CSP 4-49
1	Bergere, L.M.	CSP 4-49
1	Buchta, J.C.	CSP 4-58
2	Burnham, G.T.	CSP 4-49
1	Chun, M.K.	EP 3-221
1	Friedman, D.B.	CSP 4-49
1	Gall, D.M.	CSP 4-49
1	McJilton, T.	CSP 4-49
1	Squires, W.F.	CSP 3-2
1	Stogran, E.M.	CSP 4-49
1	Willis, P.A.	CSP 3-12
1	Gilstein, J.	Adv. Laser Systems Re-Entry Sys Dept 3198 Chestnut St. King of Prussia, Pa. 19101
1	Hulme, G.	Mail Drop 805 P.O. Box 5000 Binghamton, N.Y.
1	White, D.R.	Building, K1, Room 5A42 DR&D Schenectady, N.Y.

Copies	Name	Location
1	Brown, D.	Laboratory for Laser Energetics 250 E. River Rd. Rochester, N.Y. 14623
1	Lubin, M.	Laboratory for Laser Energetics 250 E. River Rd. Rochester, N.Y. 14623
1	Seka, W.	Laboratory for Laser Energetics 250 E. River Rd. Rochester, N.Y. 14623
1	Soures, J.	Laboratory for Laser Energetics 250 E. River Rd. Rochester, N.Y. 14623

LIST OF ILLUSTRATIONS

Figure	Title	Page
1	After SF-7, 5 $\mu J/cm^2$ (1.3 μJ)	8
2	After SF-7, 6 $\mu J/cm^2$ (1.6 μJ)	8
3	After 90-mm Amplifier, 6 $\mu J/cm^2$	8
4	After 40-mm Amplifier, 6 $\mu J/cm^2$	8
5	After First 64-mm Amplifier, 6 $\mu J/cm^2$	8
6	After Second 64-mm Amplifier, 6 $\mu J/cm^2$	8
7	After Third 64-mm Amplifier, 6 $\mu J/cm^2$	8
8	After 90-mm Amplifier, 6 $\mu J/cm^2$	8
9	5 $\mu J/cm^2$	9
10	6 $\mu J/cm^2$	9
11	5 $\mu J/cm^2$	9
12	6 $\mu J/cm^2$	9
13	6.5 $\mu J/cm^2$ → 39.19 J	9
14	6.0 $\mu J/cm^2$ → 39.61 J	9
15	5.0 $\mu J/cm^2$ → 38.28 J	9
16	4.5 $\mu J/cm^2$ → 36.34 J	10
17	4.0 $\mu J/cm^2$ → 33.69 J	10
18	3.0 $\mu J/cm^2$ → 27.01 J	10
19	2.0 $\mu J/cm^2$ → 19.13 J	10
20	1.0 $\mu J/cm^2$ → 10.20 J	10
21	0.5 $\mu J/cm^2$ → 5.28 J	10
22	Output vs Input Energy at 50 pps	10
23	20.0 $\mu J/cm^2$ → 73.98 J	11
24	18.0 $\mu J/cm^2$ → 74.75 J	11
25	16.0 $\mu J/cm^2$ → 74.24 J	11
26	12.0 $\mu J/cm^2$ → 70.90 J	11
27	9.0 $\mu J/cm^2$ → 61.12 J	11
28	7.0 $\mu J/cm^2$ → 51.87 J	11
29	6.0 $\mu J/cm^2$ → 46.51 J	11
30	5.0 $\mu J/cm^2$ → 40.64 J	11
31	4.0 $\mu J/cm^2$ → 34.19 J	11

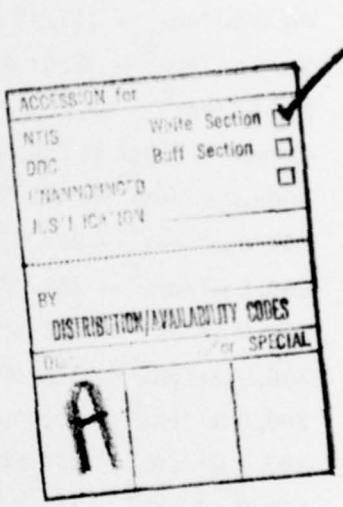

LIST OF ILLUSTRATIONS (Cont)

Figure	Title	Page
32	Output vs Input Energy at 100 pps	12
33	Temporal Evolution of Output Radial Beam at 0.08 r/r_o	12
34	80.0 $\mu J/cm^2$ → 144.77 J	12
35	70.0 $\mu J/cm^2$ → 141.84 J	12
36	60.0 $\mu J/cm^2$ → 139.12 J	12
37	52.0 $\mu J/cm^2$ → 136.47 J	12
38	48.0 $\mu J/cm^2$ → 134.65 J	12
39	44.0 $\mu J/cm^2$ → 132.28 J	12
40	40.0 $\mu J/cm^2$ → 129.20 J	13
41	36.0 $\mu J/cm^2$ → 125.28 J	13
42	30.0 $\mu J/cm^2$ → 117.47 J	13
43	20.0 $\mu J/cm^2$ → 98.01 J	13
44	5.0 $\mu J/cm^2$ → 40.65 J	13
45	Output vs Input at 200 pps	13
46	1000.0 $\mu J/cm^2$ → 272.96 J	14
47	850.0 $\mu J/cm^2$ → 267.77 J	14
48	650.0 $\mu J/cm^2$ → 258.76 J	14
49	500.0 $\mu J/cm^2$ → 249.43 J	14
50	400.0 $\mu J/cm^2$ → 241.07 J	14
51	300.0 $\mu J/cm^2$ → 229.73 J	14
52	200.0 $\mu J/cm^2$ → 212.66 J	15
53	100.0 $\mu J/cm^2$ → 180.63 J	15
54	50.0 $\mu J/cm^2$ → 145.62 J	15
55	10.0 $\mu J/cm^2$ → 66.02 J	15
56	5.0 $\mu J/cm^2$ → 40.65	15
57	Output vs Input Energy at 1 ns	15
58	Output vs Input Energy and B, ΔB at 50 ps	16
59	Output vs Input Energy and B, ΔB at 100 ps	16
60	Output vs Input Energy and B, ΔB at 200 ps	16
61	Output vs Input Energy and Flux at 1 ns	16

LIST OF ILLUSTRATIONS (Cont)

Figure	Title	Page
62	Output Power vs Input Energy	17
63	Output Power vs Input Energy and $\Delta B_{90} = 2.5$	17
64	Output Power vs Input Energy, Compressed Scale	17
65	Output Power vs Input Energy Showing Effects of B-Integral on the System	17
66	System Output Performance	17

GLOSSARY

CA	Clear aperture
ESU	Electrostatic Unit
FWHM	Full width at half maximum intensity
GDL	Glass development laser
Np	Neper
ns	nanoseconds
ps	picoseconds
SNAAP	Synthesized Neodymium Amplifier Analysis Program
TW	Terawatt

A Preliminary Analysis of GDL Performance for Short and Long Pulse Operation

The development of a three-dimensional gain code for system performance predictions has been accomplished. This code, Synthesized Neodymium Amplifier Analysis Program (SNAAP), has been used to predict the operating performance of the University of Rochester's Glass Development Laser (GDL). In its present form, the code essentially traces the propagation of a laser pulse represented by a three-dimensional matrix through a given optical system.

For the GDL system a pulse whose spatial and temporal waveforms were initially gaussian was convolved with a spatially apodizing function and then propagated through the system. The pulse is represented by a matrix (m, n, j). Each m^{th} x n^{th} x j^{th} beam element represents an intensity (w/cm^2). The code then propagates each such element and operates on it according to the type and sequence of components. Physically there are three types of optical components:

1. Amplifiers which include all gain media where passive and reflective losses are calculated where indicated.
2. Spatial filters where an assumed transfer function operates on each beam element and readjusts its intensity accordingly.
3. Attenuators which include all other optical elements such as lenses, polarizers, Pockels' cells, etc.

In its present form, most calculated parameters including B-integral (both total and delta B per stage), each intensity (m^{th} x n^{th} x j^{th}), etc. are stored in arrays for future calculations or manipulation. A great deal of flexibility and universality has been built into the code to enable both present and future users ease of modification and an understanding of the codes operation.

The input parameters used for this preliminary analysis appear in Table 1. The stored energy density profiles for each amplifier are input in the format

$$E_s(r') = E_1 + E_2 r'^P \qquad (1)$$

The specific gain for several types of Nd:doped glass (LHG-7, Q-88, ED-2, EV-2) are implemented in the code and the appropriate values used depending on the glass type specified as input.

Presently the spatial filter transmission function used for the pinhole calculation is taken from the Lawrence Livermore Laboratory 1975 Annual Report. The function used is

$$T(B) \sim \exp\left[-(B/3.4)^8\right] \tag{2}$$

Associated with each $m^{th} \times n^{th} \times j^{th}$ intensity element is a B-integral value B(m, n, j) which attenuates each intensity element at a pinhole according to Equation (2). Modifications to Equation (2) are presently being discussed and may be implemented into the code at a later date.

The effect of circular polarization is not at present contained within the code and is handled by inputting $n_2/1.5$ in place of the n_2 values listed in Table 1. Another parameter which is not presently implemented into the code is fill factor. For the purpose of simplicity, the code exactly fills the aperture of an optical element with m x n spatial elements of specified profile. As an example, suppose we have a 15-mm diameter clear aperture amplifier, area element m x n (actually intensity) is magnified by a factor of four but occupies the same relative position in amplifier II as it did in amplifier I (center transforms to center, and edge-to-edge, etc.).

In the beginning of this report it was mentioned that the spatial profile of the beam was a gaussian convoluted with a supergaussian. More specifically, the actual profile is

$$I(r) = \exp\left[-(r/0.3)^2 - (r/0.53)^{10}\right] \tag{3}$$

where r is in cm. This spatial profile is the input to the first (16-mm) amplifier. Since the fill factor is 0.26 and the code does not automatically adjust for vacuum spatial filter magnification (it adjusts for differences in clear aperture (CA) only), it is necessary to correct for the fact that the first two amplifiers (i.e. 16-mm and 30-mm) are underfilled. Basically, we wish to map the 0.001 I_o beam edge onto the edge of the 40-mm (third) amplifier. From the magnification factors listed in Table 1 this is accomplished by a simple linear transformation

$$\begin{aligned} &16 \text{ mm} \rightarrow 12.60 \text{ mm} \quad : \quad r_o' = 6.3 \text{ mm} \\ &30 \text{ mm} \rightarrow 28.99 \text{ mm} \quad : \quad r_o' = 14.5 \text{ mm} \end{aligned} \tag{4}$$

We designate these new diameters as the effective clear aperture for the respective amplifiers. The radial gain profiles for the code are all normalized to r/r_o, where r goes from 0 to r_o. In order to correctly correlate the initial beam profile with the amplifier gain

profile, it is necessary to transform the initial stored energy density profiles such that from Equation (1) we have

$$E'_2 = E_2(0.79)^{1.75} = 0.16 \qquad (5)^*$$

for the 16-mm amplifier, and

$$E'_2 = E_2(0.97)^{2.87} = 0.12 \qquad (6)^*$$

for the 30-mm amplifier.

Besides the system output parameters provided by the code, numerous component operating parameters are provided at each optical interface. Due to the large number of system components, the latter are provided mainly as a diagnostic feature. Once the system components are specified, the basic input to the code is the initial beam intensity. The code calculates numerically.

$$E_o = \int\int\int I_i(r, \theta, t)\, dr\, d\theta\, dt$$

where

E_o = Output pulse energy

I_i = Input intensity profile

The first code runs for the GDL system were at a temporal pulse length of 50 ps (FWHM). The test cases run were for inputs to the first (16-mm diameter) amplifier of 5 $\mu J/cm^2$ (1.3 μJ total beam energy) and 6 $\mu J/cm^2$ (1.6 μJ). Figures 1 and 2 are CalComp plots of the output intensity profiles after SF-7 (see Table 1) for these two cases, respectively. These graphs are the result of taking a series of 21 radial increments across the beam, propagating these through the system and adjusting the intensity of each m^{th} x n^{th} x j^{th} element for small-scale B-integral losses through the various vacuum spatial filters in the system. Figure 2 is a rather dramatic representation of the effects of B-integral on a beam focused through the pinhole of a vacuum spatial filter. Figure 3 shows a plot of the intensity profile for the same 6 $\mu J/cm^2$ input as Figure 2 but taken after the 90-mm amplifier. This is a representation of the near field of the beam. One can also see the spatial and temporal evolution of the beam (for the 6 $\mu J/cm^2$ input case) from Figures 4 through 8 inclusive). These are plots of the intensity profiles for the 40-mm, first 64-mm, second

*The primes denote the effective values of E_2 from $E_s(r/r_o) = E_1 + E'_2(r/r_o)^p$, see Equation (1).

64-mm, third 64-mm and the 90-mm amplifier, respectively. The radial stored energy density profiles for these amplifiers account for the higher intensities on the edge of the beam. Figures 9 and 10 are plots of the output energy densities as a function of normalized radial beam position for the 5 $\mu J/cm^2$ and 6 $\mu J/cm^2$ runs, respectively. Again the outputs plotted are those through SF-7 (see Table 1). As mentioned before, associated with each beam intensity element is a B-integral element B(m, n, j). Figures 11 and 12 are plots of the system B-integral values for these two runs, respectively.

The final GDL system output energy is obtained by integrating the beam intensity profile in both space and time. This is accomplished by integrating the functions appearing in Figures 9 and 10. After performing the required integration, values of 40.1 J for the 5 $\mu J/cm^2$ case and 43.1 J for the 6 $\mu J/cm^2$ case were obtained. Due to the long computing time necessary to run test cases of 21 spatial points across the beam, it was decided that for sufficient accuracies four points across the beam would be adequate to predict system performance. These points are 0, 0.35, 0.8, and 1.0 r/r_o. Note from Figure 9 that the peak occurs at the 0.8 r/r_o point. The difference in integrations of 4 points vs 21 points is 4.7%. For the 6 $\mu J/cm^2$ case, the difference is 8.9%; however, in this case the maximum does not occur at the 0.8 r/r_o radial point due to B-integral considerations. In any event, the 4-point integration produces more pessimistic results than the 21-point case.

In Table 2, the output energy vs input energy for the four temporal cases run (viz. 50 ps, 100 ps, 200 ps, and 1 ns) is presented.

Figures 13 through 21 inclusive present the beam output energy density through SF-7 (see Table 1) as a function of radius for the nine input energies at 50 ps listed in Table 2. The vertical axis is in J/cm^2 and the beam radius is normalized to one. Table 2 presents the input in J whereas in several places, such as the plots mentioned above, the input is given in J/cm^2. The assumed conversion for the two has been calculated to be 0.2626 cm^2 (the beam effective aperture area at the input to the 16-mm diameter amplifier). The plots in Figures 13 through 21 are in descending order of output energy (or input energy density). Figures 13 through 15 clearly show the effects of B-integral through SF-7 (see Table 1). The peak output energy density for the 6.5 $\mu J/cm^2$ input case is 0.82 J/cm^2 at the edge (0.8 r/r_o); however, for the 5 $\mu J/cm^2$ case, the output energy at 0.8 r/r_o is 0.88 J/cm^2. Figure 22 is a plot of the output energy as a function of input energy for the nine cases run at 50 ps. Similar data for the other three temporal runs is presented (see Table 2). Only brief mention of some interesting points of these runs will be made since many of the above comments apply for all four temporal pulse lengths. Because of the effects of the vacuum

spatial filters, the output radial beam profile (at 100 ps) is almost flat for the 20 $\mu J/cm^2$ input case (see Figure 23). This is due to the higher intensity at the 0.8 r/r_o beam radius. Figure 33 is a plot of the temporal evolution of this pulse at the 0.8 r/r_o point. The severe dip in the center of the pulse occurs due to focusing through SF-7. Figure 32 is a plot of the output energy vs input energy for the 100-ps case (see Table 2). Figures 34 through 44 inclusive contain plots of the output energy density profiles of the 11 cases at 200 ps listed in Table 2, with Figure 45 showing the output vs input energy curve for these cases. Finally, 11 cases for an input pulse width of 1 ns were run. The output energy density (through SF-7) for these cases is plotted in Figures 46 through 56 inclusive. For this case, the output is saturation flux limited and not B-integral limited as in the previous three cases. As an example, the highest input energy, 1000 $\mu J/cm^2$ (263 μJ), has a ΔB through the last amplifier stage (SF-7) of 1.37. However, the assumed flux limit of 4 J/cm^2 is exceeded at the output of the second 64-mm rod amplifier. Assuming a system could tolerate a higher flux than 4 J/cm^2 at any surface (say, for example, 6 J/cm^2), it is interesting to note that the gain of the second 64-mm amplifier is down by a factor of four from the small signal gain. At such high fluxes, the concept of gain reduces to considering an amplifier as an additive medium, rather than a gain medium; i.e.,

$$E = G\,E_o \overset{\text{high flux}}{\underset{\text{limit}}{\rightleftharpoons}} \qquad E = E_o + \Delta E$$

Although both of the above expressions are appropriate in either case, the latter is more useful at high incident flux levels. In order to insure that no system component exceeds the flux limit (4 J/cm^2) the input energy density must not exceed 145 $\mu J/cm^2$. At an input of 100 $\mu J/cm^2$ (26 μJ) the 90-mm amplifier's gain is down by almost a factor of three from the small signal gain. This is pointed out to illustrate the fact that the GDL system as presently configured is saturation flux limited under long pulse operation ($\gtrsim$ 1 ns) at low input energies ($\gtrsim$1 μJ input). This point will not be dwelt upon here but the results of saturation will be presented graphically later on in this report.

For each of the four temporal pulse length cases analyzed (50 ps, 100 ps, 200 ps, and 1 ns) input vs output energy is plotted (Figures 58 through 61). Each graph also shows the total B-integral values (Np) for the system (at the output of SF-7), as well as the delta B-integral through the last stage (SF-6 to SF-7 "pinhole to pinhole"; see Table 1). In each case values of B-integral vs input energy for the center (0.0 r/r_o) of the pulse and the edge (0.8 r/r_o) have been plotted. The latter in all cases is the higher of the two plots. Finally, the plots have been taken and system output energy vs ΔB (last stage) = 2.5 has been cross correlated. This value was chosen conservatively and is an indication of system

performance at this given B-integral limit. It is interesting to note (although it is not obvious from the graph) that for the 200-ps case (Figure 60), the system total B-integral (ΣB on the plot (center vs edge)) crosses over for high values of input energy, typically at $E_{in} \geq 16\ \mu J$ where the ΣB is the same for both center and edge. This crossover is not shown in Figure 60 since the plot does not extend beyond a 12 μJ input energy. Figure 61 is again similar to the previous three; however, in this case the flux (J/cm^2) rather than the B-integral for both the center and the edge points has been plotted. This is the limiting case for long pulse operation of GDL since the B-integral values are intensity-dependent; and due to saturation at long temporal pulse length, the intensity is considerably reduced from that of the shorter pulses. This is evident in Figure 62. Input energy with varying scales of μJ corresponding to the differences in pulse length is plotted vs output peak power. By appropriate choice of scale the vertical axis corresponds to constant output power at any of the pulse lengths (full scale represents 0.8 TW). The dashed line on this graph represents the small signal gain of the system. Although both B-integral and saturation effects are competing for depleting constant system output gain for the 50- , 100- and 200-ps cases, it is still obvious that saturation effects account for a portion of the 10% loss in output power for the 100-ps case over the 50-ps case (at the peak) and the approximate 20% loss for the 200-ps case over the 100-ps case. The saturation effects for the 1 ns case are quite obvious. Here the B-integral effects are negligible since even at the highest input energy case, 1000 $\mu J/cm^2$ (263 μJ). the total system B-integral is only 4.1 with a ΔB (all B-integrals are maximum spatial and temporal) through the last stage (SF-7) of 1.4.

Figure 63 is similar to Figure 62 except here $\Delta B = 2.5$ has been plotted through the last stage (ΔB_{90}) for the three shortest temporal pulse length cases (50 ps, 100 ps, and 200 ps). In terms of the 1-ns run the flux limit of 4 J/cm^2 is indicated. Beyond this point, saturation effects are so limiting that even if new substrates withstanding higher flux were found very little additional output could be derived from this system. To illustrate this more graphically Figure 64 is presented, which has a compressed horizontal axis. Here it is shown for the aforementioned run that at an input of 50 $\mu J/cm^2$ a fourfold increase in input energy yields an approximate 15% increase in output power.

One final run for the GDL system will be made at 500 ps for the present operating parameters (Table 1). This run should supply the data necessary to establish the following:

1. Is the $\Delta B_{90} = 2.5$ cross plot of system performance (Figure 63) a straight line?

2. Where is the crossover point for flux limit vs B-integral limit?

When this run is made, the results will be issued as an addendum to this report.

In Figure 65 plots of the output of GDL prior to SF-7 have been added to the previous information contained in Figure 63 in order to illustrate the effects of B-integral on the system.

The overall system performance is given in Figure 66, where on-target* output energy and output peak power are plotted as a function of input pulse length full width half maximum (FWHM). The output energy increases linearly below 200 ps, with a maximum of 200 J at 1 ns limited by the saturation gain of the amplifiers. The maximum peak power of the system is 0.7 TW for short pulse lengths of 50 ps or less. This peak power is limited by the action of the final spatial filter.

In summary the GDL system as configured in Table 1 (one arm of OMEGA-10) will produce the following outputs (see Figure 66):

0.7 TW at 50 ps
0.65 TW at 100 ps
0.6 TW at 200 ps
200 J at 1 ns

Consequently, OMEGA-10 up to and including the 90-mm diameter amplifiers will produce:

16.8 TW at 50 ps
15.6 TW at 100 ps
14.4 TW at 200 ps
4.8 kJ at 1 ns

*Focusable within 500 μrad.

OUTPUT INTENSITY PROFILES

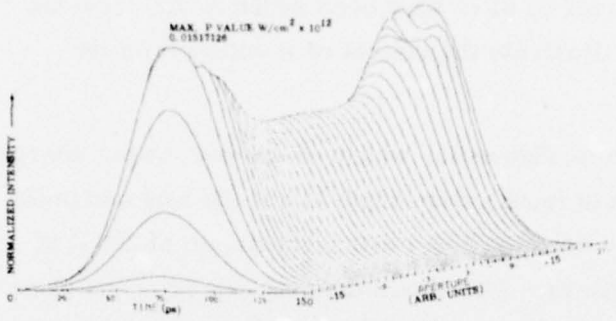

Fig. 1. After SF-7, 5 $\mu J/cm^2$ (1.3 μJ)

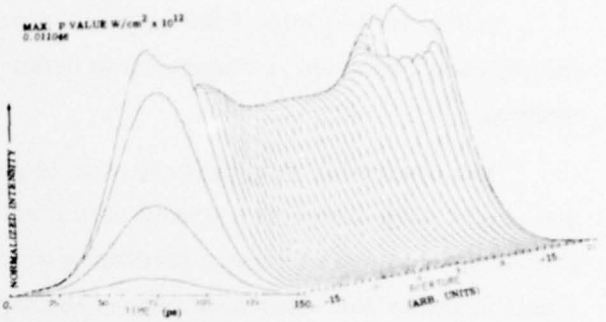

Fig. 2. After SF-7, 6 $\mu J/cm^2$ (1.6 μJ)

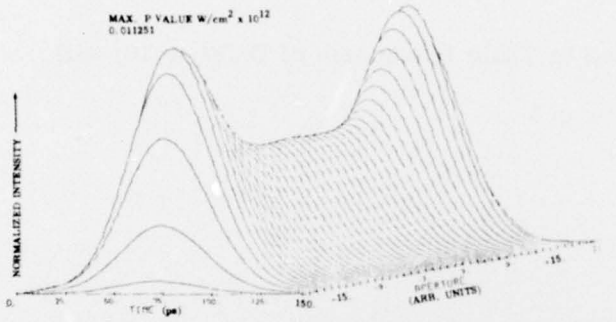

Fig. 3. After 90-mm Amplifier, 6 $\mu J/cm^2$

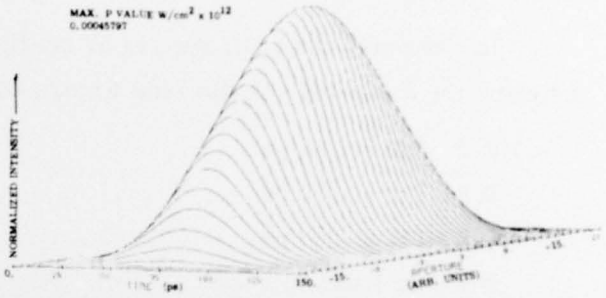

Fig. 4. After 40-mm Amplifier, 6 $\mu J/cm^2$

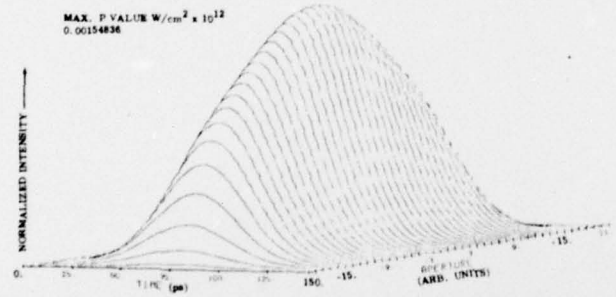

Fig. 5. After First 64-mm Amplifier, 6 $\mu J/cm^2$

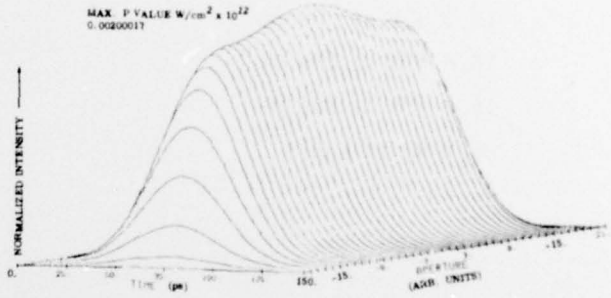

Fig. 6. After Second 64-mm Amplifier, 6 $\mu J/cm^2$

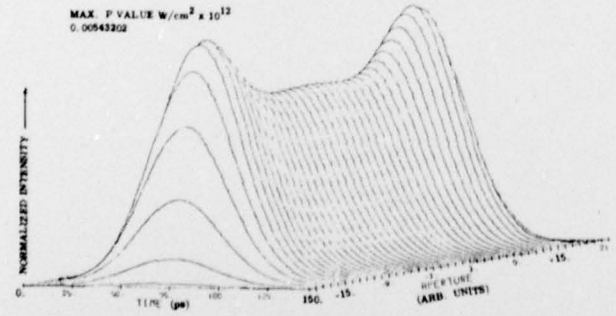

Fig. 7. After Third 64-mm Amplifier, 6 $\mu J/cm^2$

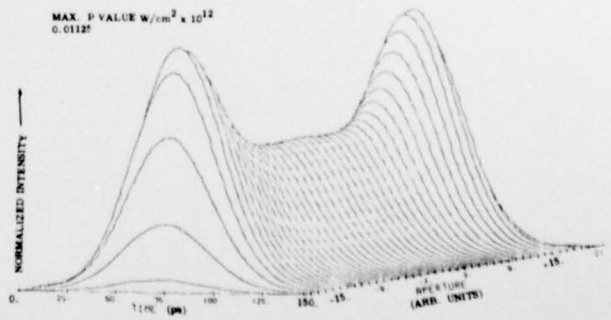

Fig. 8. After 90-mm Amplifier, 6 $\mu J/cm^2$

OUTPUT ENERGY DENSITIES AS A FUNCTION OF RADIUS THROUGH SF-7

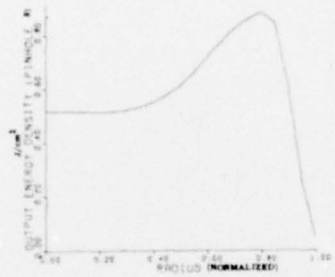

Fig. 9. 5 $\mu J/cm^2$

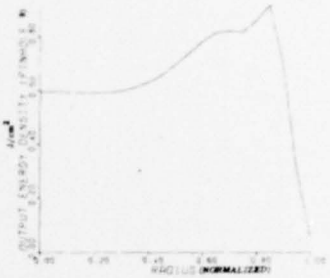

Fig. 10. 6 $\mu J/cm^2$

SYSTEM B-INTEGRALS

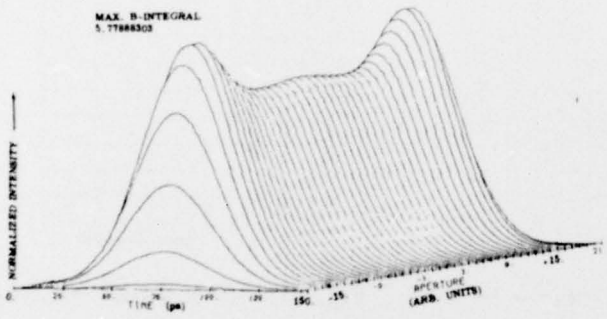

Fig. 11. 5 $\mu J/cm^2$

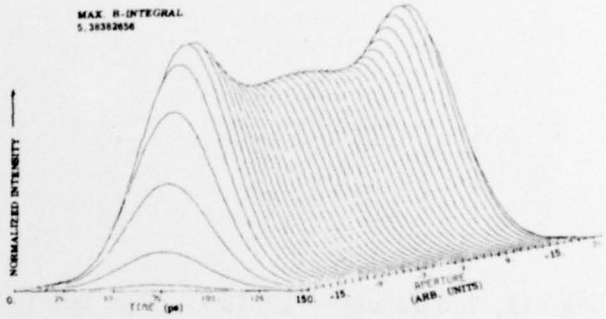

Fig. 12. 6 $\mu J/cm^2$

OUTPUT ENERGY DENSITIES AS A FUNCTION OF RADIUS AT 50 ps

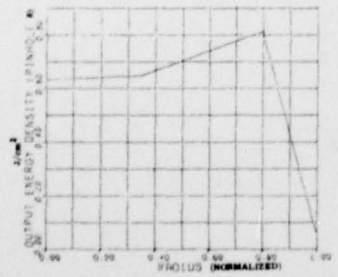

Fig. 13. 6.5 $\mu J/cm^2 \rightarrow 39.19$ J

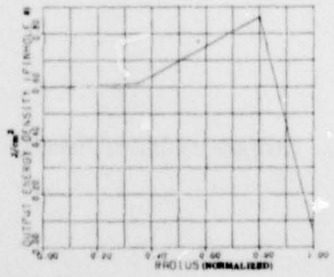

Fig. 14. 6.0 $\mu J/cm^2 \rightarrow 39.61$ J

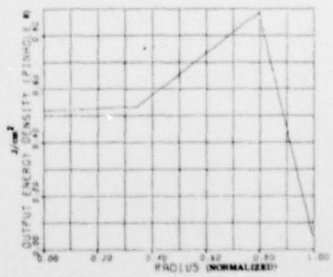

Fig. 15. 5.0 $\mu J/cm^2 \rightarrow 38.28$ J

OUTPUT ENERGY DENSITIES AS A FUNCTION OF RADIUS AT 50 ps (Cont)

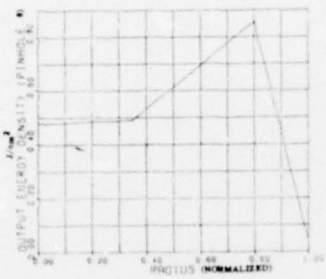

Fig. 16. 4.5 $\mu J/cm^2 \rightarrow 36.34$ J

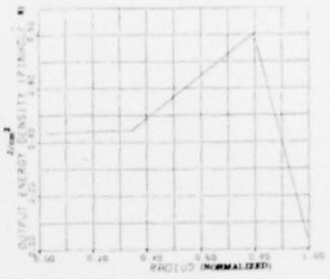

Fig. 17. 4.0 $\mu J/cm^2 \rightarrow 33.69$ J

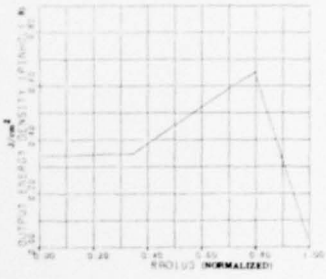

Fig. 18. 3.0 $\mu J/cm^2 \rightarrow 27.01$ J

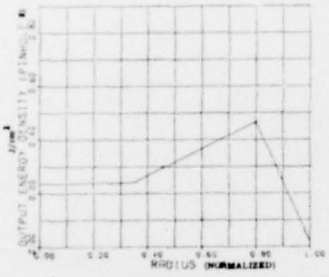

Fig. 19. 2.0 $\mu J/cm^2 \rightarrow 19.13$ J

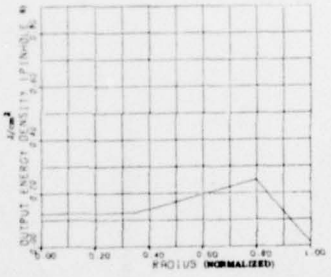

Fig. 20. 1.0 $\mu J/cm^2 \rightarrow 10.20$ J

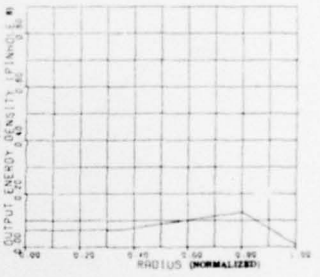

Fig. 21. 0.5 $\mu J/cm^2 \rightarrow 5.28$ J

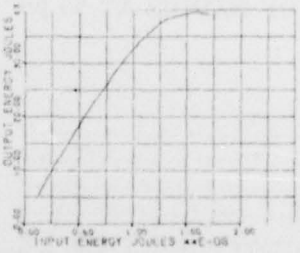

Fig. 22. Output vs Input Energy at 50 ps

OUTPUT ENERGY DENSITIES AS A FUNCTION OF RADIUS AT 100 ps

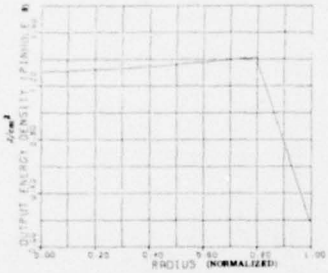

Fig. 23. 20.0 $\mu J/cm^2 \rightarrow$ 73.98 J

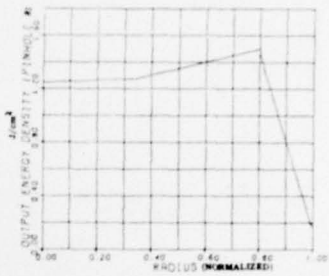

Fig. 24. 18.0 $\mu J/cm^2 \rightarrow$ 74.75 J

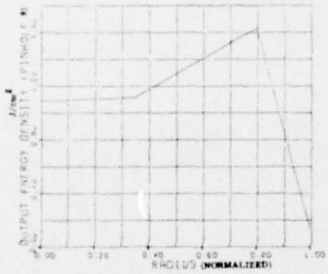

Fig. 25. 16.0 $\mu J/cm^2 \rightarrow$ 74.24 J

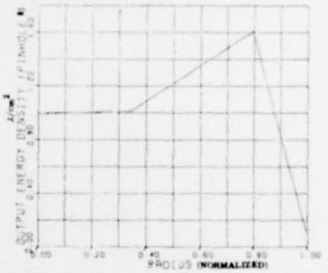

Fig. 26. 12.0 $\mu J/cm^2 \rightarrow$ 70.90 J

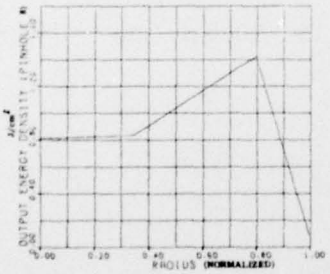

Fig. 27. 9.0 $\mu J/cm^2 \rightarrow$ 61.12 J

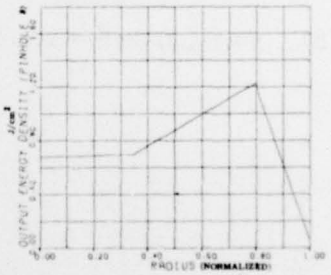

Fig. 28. 7.0 $\mu J/cm^2 \rightarrow$ 51.87 J

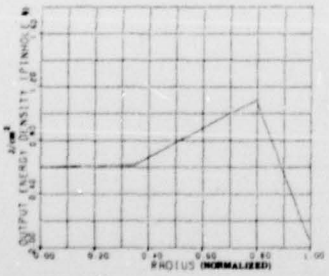

Fig. 29. 6.0 $\mu J/cm^2 \rightarrow$ 46.51 J

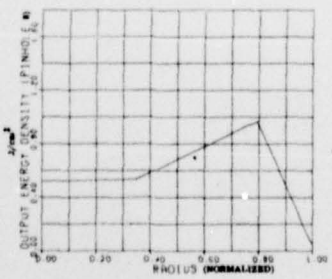

Fig. 30. 5.0 $\mu J/cm^2 \rightarrow$ 40.64 J

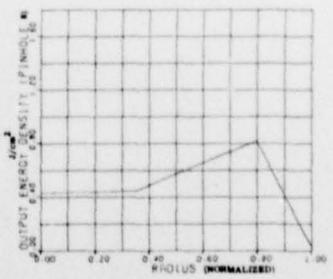

Fig. 31. 4.0 $\mu J/cm^2 \rightarrow$ 34.19 J

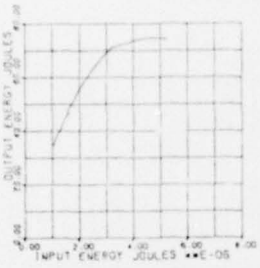

Fig. 32. Output vs Input Energy at 100 ps

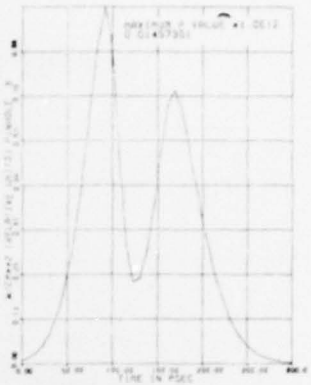

Fig. 33. Temporal Evolution of Output Radial Beam at 0.8 r/r_o

OUTPUT ENERGY DENSITIES AS A FUNCTION OF RADIUS AT 200 ps

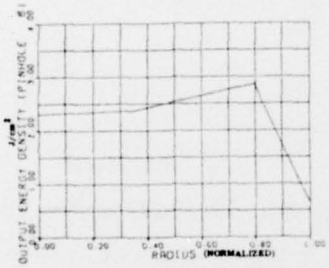

Fig. 34. 80.0 $\mu J/cm^2 \rightarrow$ 144.77 J

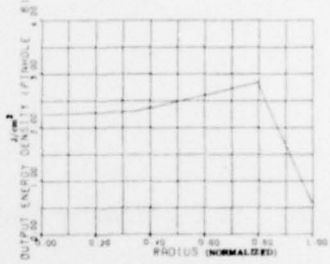

Fig. 35. 70.0 $\mu J/cm^2 \rightarrow$ 141.84 J

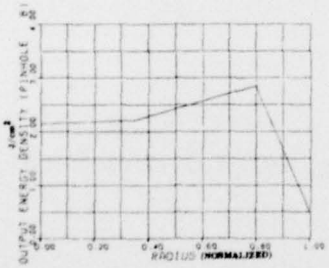

Fig. 36. 60.0 $\mu J/cm^2 \rightarrow$ 139.12 J

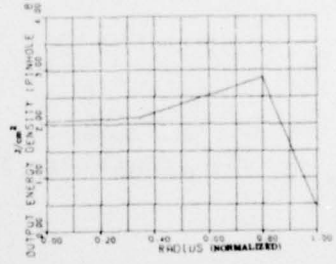

Fig. 37. 52.0 $\mu J/cm^2 \rightarrow$ 136.47 J

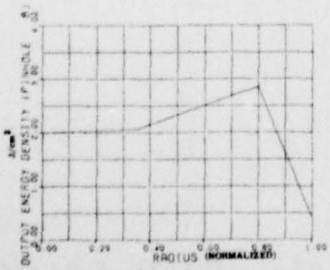

Fig. 38. 48.0 $\mu J/cm^2 \rightarrow$ 134.65 J

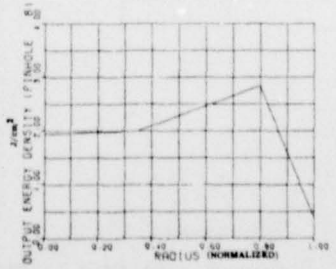

Fig. 39. 44.0 $\mu J/cm^2 \rightarrow$ 132.28 J

OUTPUT ENERGY DENSITIES AS A FUNCTION OF RADIUS AT 200 ps (Cont)

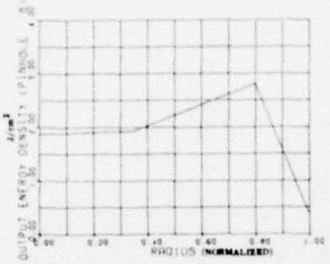

Fig. 40. 40.0 $\mu J/cm^2 \rightarrow 129.20$ J

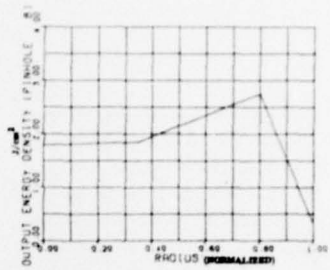

Fig. 41. 36.0 $\mu J/cm^2 \rightarrow 125.28$ J

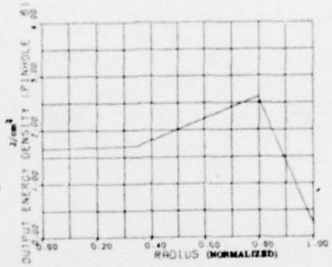

Fig. 42. 30.0 $\mu J/cm^2 \rightarrow 117.47$ J

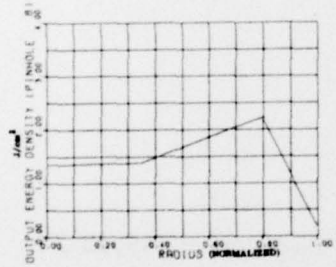

Fig. 43. 20.0 $\mu J/cm^2 \rightarrow 98.01$ J

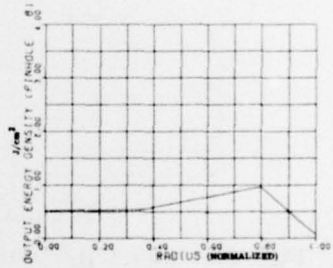

Fig. 44. 5.0 $\mu J/cm^2 \rightarrow 40.65$ J

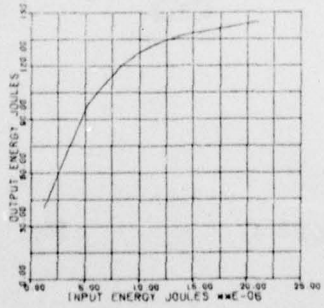

Fig. 45. Output vs Input at 200 ps

OUTPUT ENERGY DENSITIES AS A FUNCTION
OF RADIUS AT 1 ns

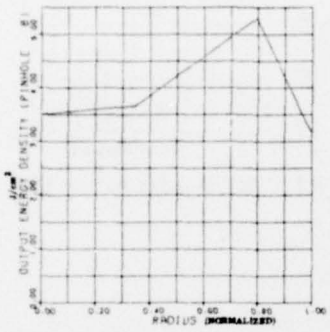

Fig. 46. 1000.0 $\mu J/cm^2 \rightarrow$ 272.96 J

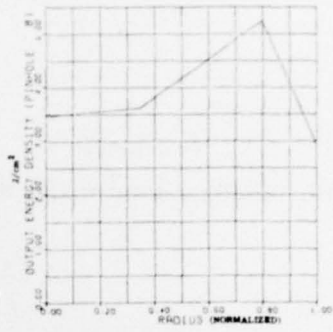

Fig. 47. 850.0 $\mu J/cm^2 \rightarrow$ 267.77 J

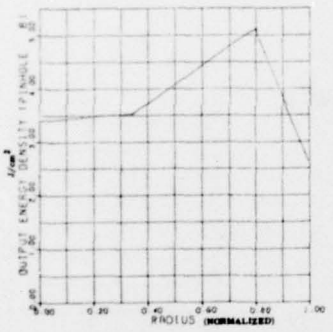

Fig. 48. 650.0 $\mu J/cm^2 \rightarrow$ 258.76 J

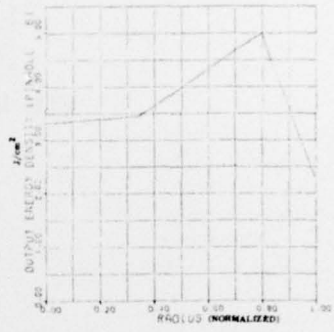

Fig. 49. 500.0 $\mu J/cm^2 \rightarrow$ 249.43 J

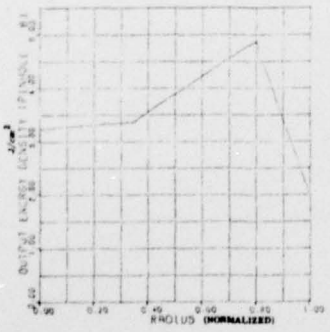

Fig. 50. 400.0 $\mu J/cm^2 \rightarrow$ 241.07 J

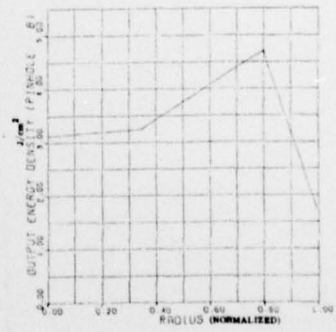

Fig. 51. 300.0 $\mu J/cm^2 \rightarrow$ 229.73 J

OUTPUT ENERGY DENSITIES AS A FUNCTION OF RADIUS AT 1 ns (Cont)

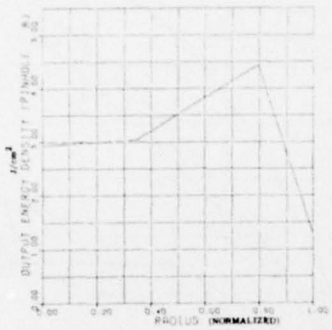

Fig. 52. 200.0 $\mu J/cm^2 \rightarrow 212.66$ J

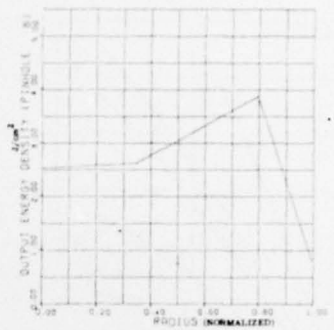

Fig. 53. 100.0 $\mu J/cm^2 \rightarrow 180.63$ J

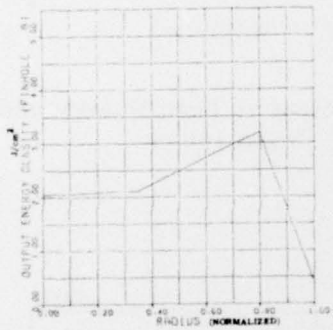

Fig. 54. 50.0 $\mu J/cm^2 \rightarrow 145.62$ J

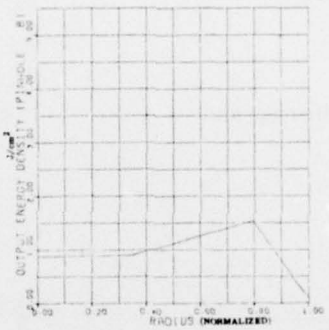

Fig. 55. 10.0 $\mu J/cm^2 \rightarrow 66.02$ J

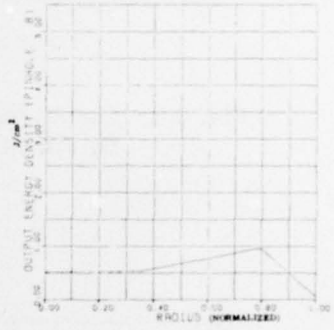

Fig. 56. 5.0 $\mu J/cm^2 \rightarrow 40.65$

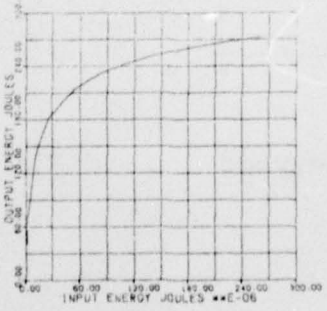

Fig. 57. Output vs Input Energy at 1 ns

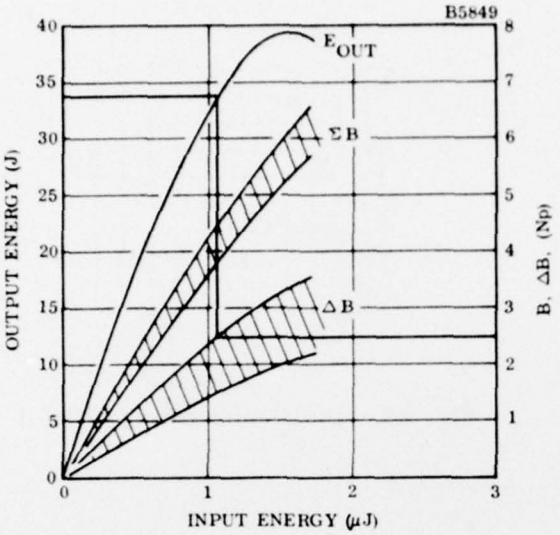

Fig. 58. Output vs Input Energy and B, ΔB at 50 ps

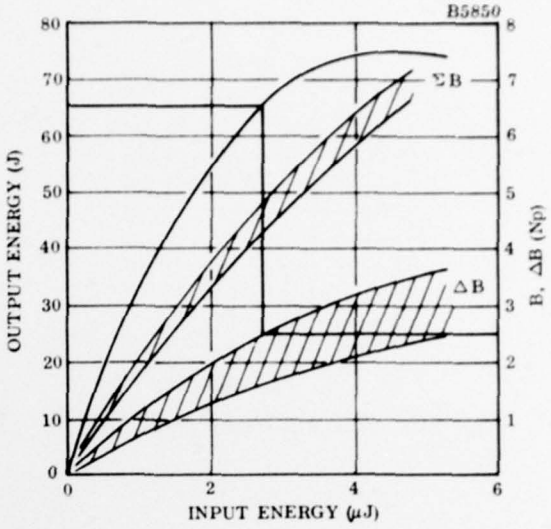

Fig. 59. Output vs Input Energy and B, ΔB at 100 ps

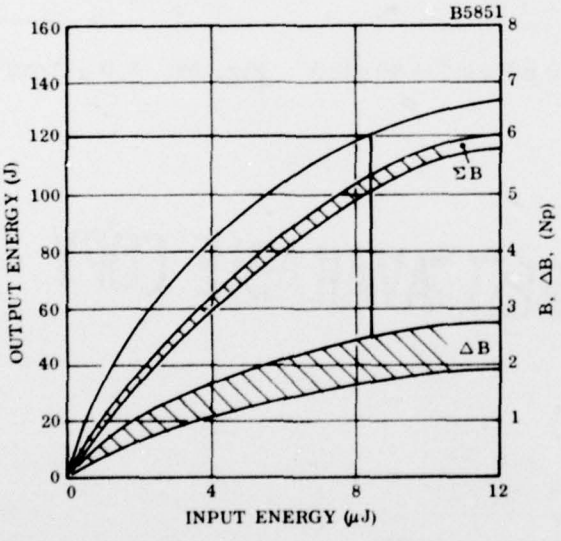

Fig. 60. Output vs Input Energy and B, ΔB at 200 ps

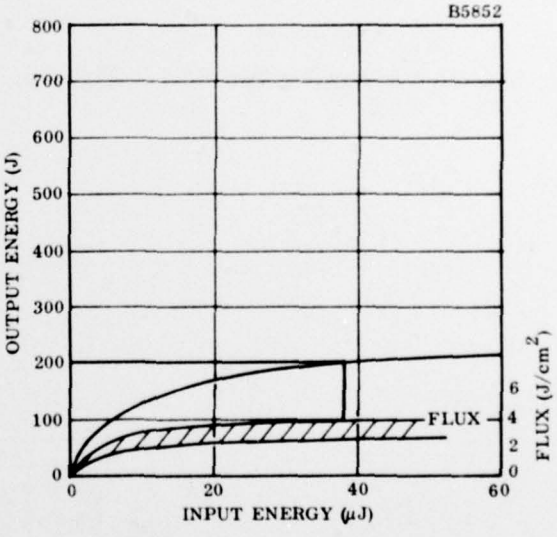

Fig. 61. Output vs Input Energy and Flux at 1 ns

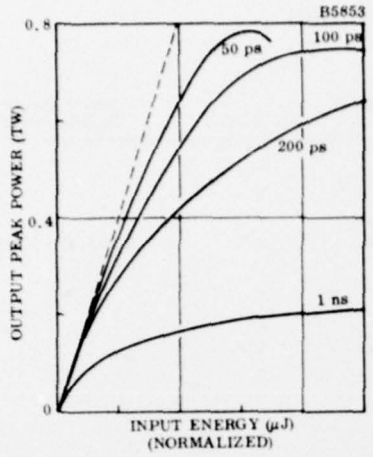

Fig. 62. Output Power vs Input Energy

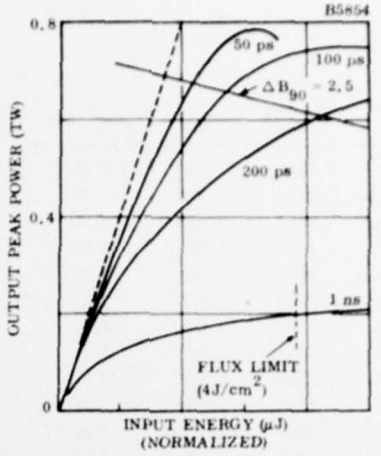

Fig. 63. Output Power vs Input Energy and $\Delta B_{90} = 2.5$

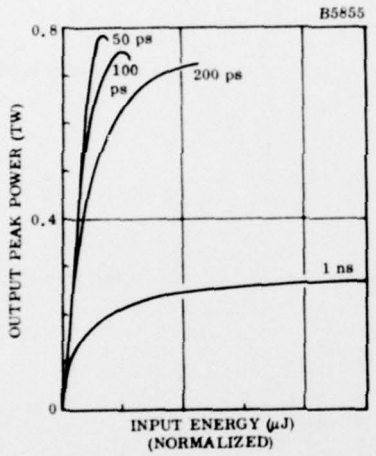

Fig. 64. Output Power vs Input Energy, Compressed Scale

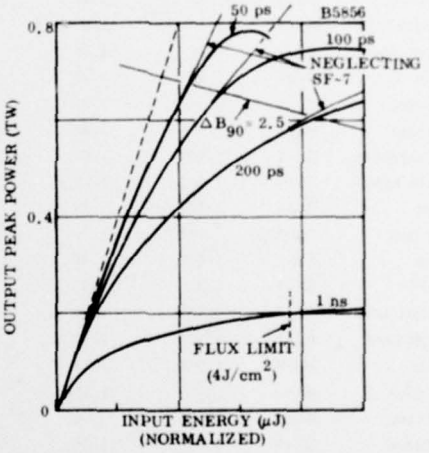

Fig. 65. Output Power vs Input Energy Showing Effects of B-Integral on the System

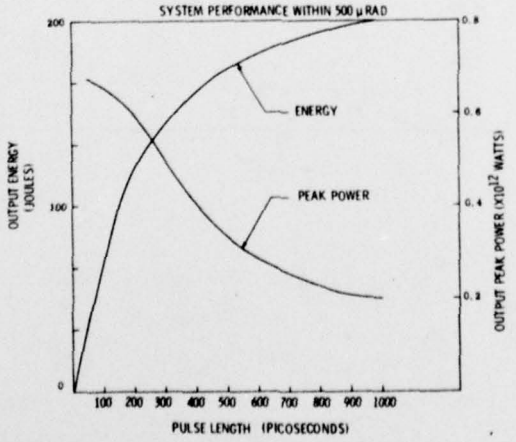

Fig. 66. System Output Performance

TABLE 1. INPUT PARAMETERS

Component	Material Type	n_0	$n_2(10^{-13}$ esu)	Thickness (cm)	Active Pump Length (cm)	Diameter (mm)	Polarization	Stored Energy Density Profile
Polarizer	BK-7	1.507	1.24	1.0			L	
SF-7 Output Lens	BK-7	1.507	1.24	1.0			C	
SF-8 Input Lens	BK-7	1.507	1.24	1.0			C	
90 mm Ampl	EV-2	1.50	0.95	37	30	90	C	$\alpha = 0.25(0.25 + 0.193\ r^4)$
SF-7 Output Lens	BK-7	1.507	1.24	1.0			C	
SF-7 Input Lens	BK-7	1.507	1.24	1.0			C	
Polarizer	BK-7	1.507	1.24	1.0			L	
PC5-Window	BK-7	1.507	1.24	1.0			L	
PC5-Crystal	KD*P	1.468	1.00	10.0			L	
PC5-Window	BK-7	1.507	1.24	1.0			L	
Polarizer	BK-7	1.507	1.24	1.0			L	
SF-6 Output Lens	BK-7	1.507	1.24	1.0			C	
SF-6 Input Lens	BK-7	1.507	1.24	1.0			C	
64III Ampl	EV-2	1.50	0.95	37	30	64	C	$\alpha = 0.25(0.36 + 0.173\ r^{2.44})$
Beamsplitter	BK-7	1.507	1.24	1.0			L	
Beamsplitter	BK-7	1.507	1.24	1.0			L	
SF-5 Output Lens	BK-7	1.507	1.24	1.0			C	
SF-5 Input Lens	BK-7	1.507	1.24	1.0			C	
64II Ampl	Q-88	1.53	1.22	37	30	64	C	$\alpha = 0.22(0.365 + 0.173\ r^{2.5})$
Beamsplitter	BK-7	1.507	1.24	1.0			L	
Beamsplitter	BK-7	1.507	1.24	1.0			L	
SF-4 Output Lens	BK-7	1.507	1.24	1.0			L	
SF-4 Input Lens	BK-7	1.507	1.24	1.0			L	
Polarizer	BK-7	1.507	1.24	1.0			L	
Faraday Rot.	FR-4	1.556	1.95	2.54			L	
Polarizer	BK-7	1.507	1.24	1.0			L	
64I Ampl	Q-88	1.53	1.22	37	30	64	C	$\alpha = 0.22(0.365 + 0.173\ r^{2.5})$
SF-3 Output Lens	BK-7	1.507	1.24	1.0			C	
SF-3 Input Lens	BK-7	1.507	1.24	1.0			C	
Polarizer	BK-7	1.507	1.24	1.0			L	
PC-4 Window	BK-7	1.507	1.24	1.27			L	
PC-4 Crystal	KD*P	1.468	1.00	6.2			L	
PC-4 Window	BK-7	1.507	1.24	1.27			L	
Polarizer	BK-7	1.507	1.24	1.0			L	
40-mm Ampl	EV-2	1.50	0.95	37	30	40	C	$\alpha = 0.25(0.45 + 0.05\ r^2)$
SF-2 Output Lens	BK-7	1.507	1.24	1.00			C	
SF-2 Input Lens	BK-7	1.507	1.24	1.00			C	
30-mm Ampl	EV-2	1.50	0.95	37	30	30	C	$\alpha = 0.25(0.5 + 0.138\ r^{2.28})$
SF-1 Output Lens	BK-7	1.507	1.24	1.0			C	
SF-1 Input Lens	BK-7	1.507	1.24	1.0			C	
PC3 + POL's							-	
16-mm Ampl	EV-2	1.50	0.95	37	30		L	$\alpha = 0.25(0.60 + 0.3\ r^2 - 0.05\ r^4)$

TABLE 2

INPUT ENERGY VS OUTPUT ENERGY

Input (μJ)	Output (J)	Fig. Ref.
	50 ps	
1.707	39.19	13
1.575	39.61	14
1.313	38.28	15
1.182	36.34	16
1.050	33.69	17
0.788	27.01	18
0.525	19.13	19
0.263	10.20	20
0.131	5.28	21
	100 ps	
5.25	73.98	23
4.73	74.75	24
4.20	74.24	25
3.15	70.90	26
2.36	61.12	27
1.84	51.87	28
1.58	46.51	29
1.31	40.64	30
1.05	34.19	31

TABLE 2

INPUT ENERGY VS OUTPUT ENERGY (Cont)

Input (μJ)	Output (J)	Fig. Ref.
	200 ps	
21.00	144.77	34
18.38	141.84	35
15.75	139.12	36
13.65	136.47	37
12.60	134.65	38
11.55	132.28	39
10.50	129.20	40
9.45	125.28	41
7.88	117.47	42
5.25	98.01	43
1.31	40.65	44
	1 ns	
262.56	272.96	46
223.18	267.77	47
170.66	258.76	48
131.28	249.43	49
105.02	241.07	50
78.77	229.73	51
52.51	212.66	52
26.26	180.63	53
13.13	145.62	54
2.63	66.02	55
1.31	40.65	56

ACKNOWLEDGMENTS

I would like to thank O. Bakeman, GE-HMED, D. Brown, J. Soures and W. Seka, University of Rochester, LLE, for many useful discussions throughout the course of this analysis as well as the programming assistance of R. Hopper, GE-HMED.